Supporting material:

Analysis of molecular movement reveals latticelike obstructions to diffusion in heart muscle cells

Ardo Illaste, Martin Laasmaa, Pearu Peterson and Marko Vendelin
Laboratory of Systems Biology, Institute of Cybernetics, Tallinn University of Technology, Estonia

The supporting material is split into several sections. First, a brief overview of the RICS method and our extensions to it is given. Second, description of experimental methods, including confocal microscope setup is presented. Then, description of the analysis of RICS images is described and demonstrated by analyzing diffusion of molecules in water and measurement solution. Forth, description of stochastic computational model is given together with derivations used to relate barrier permeability to physical parameters of the barrier and molecule size. Lastly statistical analysis of model parameters estimation is presented.

Contents

1 RASTER IMAGE CORRELATION SPECTROSCOPY

1.1 Basics

Raster image correlation spectroscopy (RICS) is based on merging the concepts of scanning confocal microscopy, FCS and image correlation spectroscopy (1, 2). While more detailed reviews are available covering the method and how it relates to other FCS-based methods (3, 4), we here present a brief overview of the concepts behind RICS and to our modification to this method.

The fundamental idea behind RICS is the realization that in an image obtained by a laser scanning confocal microscope, pixels on the image are not only separated in space but also in time (2). Photons emitted by excited fluorescent molecules are recorded as raster images as the mirrors scan the laser beam on the specimen. When recording a two dimensional raster image, the laser beam moves along one image axis (ξ), spending τ_d seconds acquiring each pixel on the line (dwell time), then flies back to the beginning of the line with flyback time τ_f, moves one pixel forward in the other axis(ψ) and records the second line. This sequential processes is repeated until the whole image has been scanned line by line (Fig. S1A), resulting in a rectangular grid of pixels separated in space and time. By calculating the correlation function (CF) of the scanned image it is possible to extract information about the space-time relationship between the pixels and to characterize, for example, reaction kinetics, translational and rotational diffusion, conformational dynamics, molecular flow, etc. (3–5). This can be done by fitting experimentally obtained CFs with theoretical CFcurves derived for the phenomenon being observed. In this paper we focus on applying RICS on analysis of diffusion of fluorescent dyes.

The correlation function $G(\Delta\xi, \Delta\psi, \Delta\zeta)$ indicates the similarity of an image to a copy of itself shifted by $\Delta\xi$ in the ξ direction, $\Delta\psi$ in the ψ direction (see Fig. S1B) and, in case a 3D stack of images is analyzed, $\Delta\zeta$ in the ζ direction (otherwise $\Delta\zeta = 0$).

The CF for a given shift is calculated by multiplying the fluorescence values in the original image with values in the shifted image and averaging over all the pixels. The result is normalized to average image fluorescence squared:

$$G(\Delta\xi, \Delta\psi, \Delta\zeta) = \frac{\langle F(\xi,\psi,\zeta)\cdot F(\xi+\Delta\xi,\psi+\Delta\psi,\zeta+\Delta\zeta)\rangle_{\xi,\psi,\zeta}}{\langle F\rangle^2_{\xi,\psi,\zeta}} - 1, \quad (1)$$

where $\langle \ldots \rangle$ signifies averaging over the whole image.

The CF can also be calculated in terms of fluorescence fluctuations from the average $\delta F = F - \langle F\rangle$ by substituting

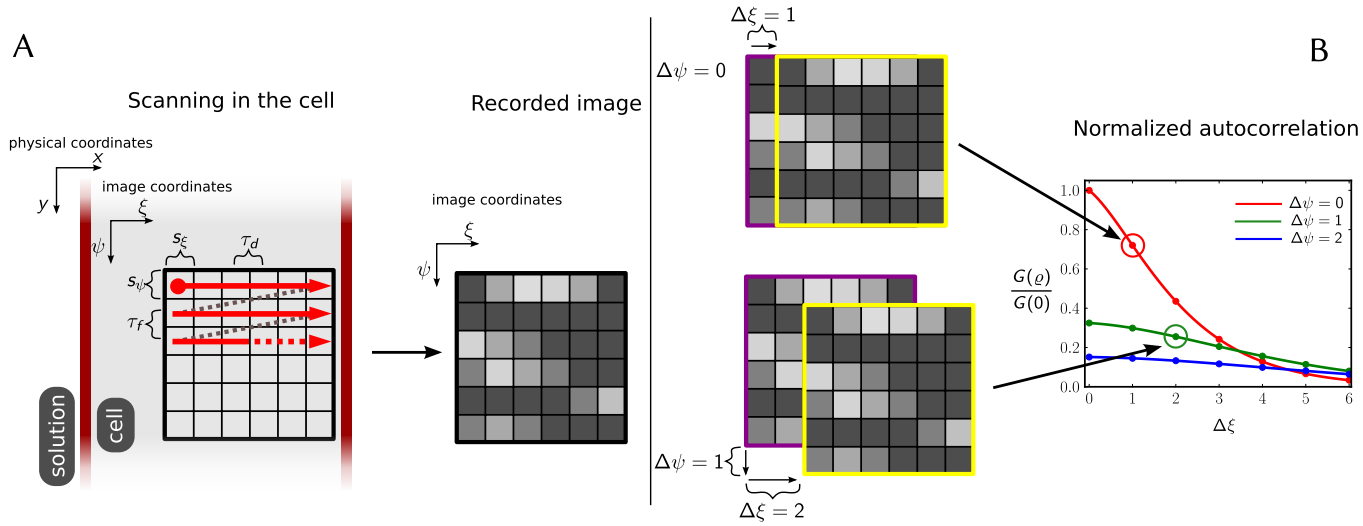

FIGURE S1: Explanation of the RICS protocol.(A) A raster image consisting of a grid of pixels is acquired within a cell. Pixels are separated by s_ξ,s_ψ μm spatially and by τ_d,$n_\xi \times \tau_d + \tau_f$ μs temporally in the ξ and ψ directions, respectively. In the default case the image coordinates ξ,ψ align with the physical coordinates x,y. The image obtained shows traces of diffusing molecules within the cell. (B)The CF $G(\boldsymbol{\varrho})$ for the shift $\boldsymbol{\varrho} = (\Delta\xi, \Delta\psi)$ is calculated by shifting a copy of the original image, multiplying the fluorescence values and averaging over the entire image. Arrows indicate the location of the correlation value for the shifts shown. The CF here is normalized to the zero-shift correlation $G(0)$ from Eq.7

$F = \delta F + \langle F \rangle$ into Eq.1:

$$G(\Delta\xi, \Delta\psi, \Delta\zeta) = \frac{\langle \delta F(\xi,\psi,\zeta) \cdot \delta F(\xi+\Delta\xi, \psi+\Delta\psi, \zeta+\Delta\zeta) \rangle_{\xi,\psi,\zeta}}{\langle F \rangle^2_{\xi,\psi,\zeta}}.$$

It is more convenient to present the CF in vector form with image shift vector $\boldsymbol{\varrho} = [\Delta\xi, \Delta\psi, \Delta\zeta]$ and position vector $\mathbf{h} = [\xi, \psi, \zeta]$:

$$G(\boldsymbol{\varrho}) = \frac{\langle \delta F(\mathbf{h}) \cdot \delta F(\mathbf{h}+\boldsymbol{\varrho}) \rangle_{\mathbf{h}}}{\langle F \rangle^2_{\mathbf{h}}}. \quad (2)$$

The physical coordinates corresponding to image coordinates $\mathbf{h}$ are $\mathbf{p} = \mathbf{p_0} + \mathbf{hS}$. Here, $\mathbf{p_0}$ is the physical location at the 0-th pixel and $\mathbf{S} = \mathrm{diag}(s_\xi, s_\psi, s_\zeta)$ is a diagonal matrix containing pixel sizes in each image dimension. Shift $\boldsymbol{\varrho}$ in image coordinates converts to a shift $\mathbf{q} = [\Delta x, \Delta y, \Delta z]$ in the physical coordinate system:

$$\mathbf{q}(\boldsymbol{\varrho}) = \boldsymbol{\varrho}\mathbf{S} = [\Delta\xi, \Delta\psi, \Delta\zeta] \begin{pmatrix} s_\xi & 0 & 0 \\ 0 & s_\psi & 0 \\ 0 & 0 & s_\zeta \end{pmatrix} = [\Delta\xi \cdot s_\xi, \Delta\psi \cdot s_\psi, \Delta\zeta \cdot s_\zeta] = [\Delta x, \Delta y, \Delta z].$$

For simplicity we consider that the fluorescence signal recorded at location $\mathbf{p}$ is obtained from the convolution of the point spread function (PSF) of the microscope and the concentration of the fluorescent dye (c) in the PSF volume.

$$F(\mathbf{p}) = B \int W(\mathbf{r}) \cdot c(\mathbf{p}-\mathbf{r})\, \mathrm{d}\mathbf{r},$$

where W is the PSF and B a parameter called brightness given by $B = q\sigma Q$ (5). Here q is the quantum efficiency of detecting emitted photons, σ the cross-section of absorption and Q the emission quantum yield of the fluorescent molecule. Employing this relationship between recorded fluorescence and concentration, Eq.2 can be used to connect the fluctuations of fluorescence visible on the recorded image to fluctuations in concentration of the diffusing dye:

$$G(\boldsymbol{\varrho}) = \frac{\langle \delta F(\mathbf{p}) \cdot \delta F(\mathbf{p}+\mathbf{q}(\boldsymbol{\varrho})) \rangle_{\mathbf{p}}}{\langle F(\mathbf{p}) \rangle^2_{\mathbf{p}}} = \frac{1}{\langle c(\mathbf{p}) \rangle^2_{\mathbf{p}}} \iint W(\mathbf{r}) W(\mathbf{r}') G_D(\mathbf{r}, \mathbf{r}', \boldsymbol{\varrho})\, \mathrm{d}\mathbf{r}\, \mathrm{d}\mathbf{r}'. \quad (3)$$

G_D is the correlation due to diffusion and can be calculated analytically (6):

$$G_D(\mathbf{r}, \mathbf{r}', \boldsymbol{\varrho}) = \langle \delta c(\mathbf{p}+\mathbf{r}) \cdot \delta c(\mathbf{p}+\mathbf{r}'+\mathbf{q}(\boldsymbol{\varrho})) \rangle_{\mathbf{p}} = \langle c \rangle \prod_{i=1}^{n} (4\pi D_i)^{-\frac{1}{2}} \exp\left(-\frac{(r_i' + q_i - r_i)^2}{4 D_i\, t(\boldsymbol{\varrho})} \right), \quad (4)$$

where $\delta c(\mathbf{p})$ is the fluctuation in concentration of the fluorescent dye at location $\mathbf{p}$, $\langle c \rangle$ is the average concentration, D_i are diagonal components of the diffusion tensor in the coordinate system composed of principal axes, collected here into $\mathbf{D} = [D_x, D_y, D_z]$. If diffusion is isotropic then all components in $\mathbf{D}$ are equal. In the case of anisotropic diffusion, components of $\mathbf{D}$ can have different values. The time delay $t(\boldsymbol{\varrho})$ indicates how much time has passed between acquisition of two pixels separated by the shift $\boldsymbol{\varrho}$. The number n indicates the number of dimensions and in general $n = 3$. The equations are still valid, however, for other n values as well.

Although the PSF is dependent on the microscope and should be measured experimentally, an analytic estimate is often used

(5, 6):

$$W(\mathbf{r}) = \prod_{i=1}^{n} \exp\left(-2\frac{r_i^2}{w_i}\right) \tag{5}$$

Here, $\mathbf{w}$ is a vector describing the width of the PSF in spatial directions. It is customary to perform calibrations using a fluorescent molecule with a known concentration in order to determine the $\mathbf{w}$ values. Furthermore, the x and y components of $\mathbf{w}$ are often assumed to be equal.

Using the PSF definition from Eq.5 and G_D from Eq.4 the integrals in Eq.2 can be calculated and the following analytic form obtained:

$$G(\boldsymbol{\varrho}) = \frac{1}{\langle c\rangle}\prod_{i=1}^{n}\left[\frac{1}{\sqrt{\pi\left(4D_i t(\boldsymbol{\varrho}) + w_i^2\right)}} \cdot \exp\left(-\frac{q(\boldsymbol{\varrho})_i^2}{4D_i t(\boldsymbol{\varrho}) + w_i^2}\right)\right]. \tag{6}$$

From this result it can be seen that with zero shift (i.e., $\boldsymbol{\varrho} = (0,0,0)$) the CF gives:

$$G(0) = \frac{1}{\langle c\rangle}\prod_{i=1}^{n}\frac{1}{\sqrt{\pi}w_i}. \tag{7}$$

As $G(0)$ is independent of the diffusion of the fluorescent molecule it can be used to determine the global concentration of the molecule or, knowing that, the properties of the PSF (i.e., components of $\mathbf{w}$).

1.2 Time delay between pixels

Scanning a 2D raster image with n_ξ pixels in the ξ direction, with τ_d seconds used as the dwell time for all pixels and τ_f being the time that it takes for the beam to move from the end of one line to the beginning of the next, the time delay between two pixels separated by the shift $\boldsymbol{\varrho}$ used in Eqs. 6 and 9 is:

$$t(\boldsymbol{\varrho}) = t(\Delta\xi, \Delta\psi) = \Delta\xi \cdot \tau_d + \Delta\psi \cdot (n_\xi \cdot \tau_d + \tau_f). \tag{8}$$

Inserting this relation in the CF Eqs. 6 and 9 will yield the function that can be used for fitting experimentally obtained data and obtaining diffusion coefficients.

1.3 Motivation for modifications

As we have demonstrated, RICS can be used to determine anisotropy of diffusion by varying the time delay between physical location in the sample during a scan. This can be achieved by altering the angle of scanning (7).

Also, diffusion dependent changes in the CF can be subtle, making them hard to detect and fit, especially with noisy data. Through changes in scanning resolution additional aspects of the CF can be estimated, leading to a larger amount of datapoints available for fitting.

1.4 Changes in scanning angle

In order to detect anisotropy of diffusion, several scanning angles can be used to alter the time delay between pixels acquired from the same location (7). When scanning is performed at an angle α relative to the physical coordinate axes, the CF equations need to be modified to account for this. For example, if scanning is performed under a 90° angle, the image ξ and ψ axes actually correspond to the physical y and x axes, respectively (see Fig. S2A). The CF that takes the scanning angle into account is:

$$G(\boldsymbol{\varrho}, \alpha) = \frac{1}{\langle c\rangle}\prod_{i=1}^{n}\left[\frac{1}{\sqrt{\pi\left(4D_i t(\boldsymbol{\varrho}) + w_i^2\right)}} \cdot \exp\left(-\frac{q(\boldsymbol{\varrho}, \alpha)_i^2}{4D_i t(\boldsymbol{\varrho}) + w_i^2}\right)\right], \tag{9}$$

where the physical shift $\mathbf{q}$ is now a function of the rotation angle α:

$$\mathbf{q}(\boldsymbol{\varrho}, \alpha) = \boldsymbol{\varrho}\mathbf{S}\left(\mathbf{M}(\alpha)\right)^T \tag{10}$$

$\mathbf{M}(\alpha)$ is the rotation matrix for rotation angle α. For rotating around the z axis, as is done in this paper, the rotation matrix is:

$$\mathbf{M}(\alpha) = \begin{pmatrix} \cos\alpha & -\sin\alpha & 0 \\ \sin\alpha & \cos\alpha & 0 \\ 0 & 0 & 1 \end{pmatrix}.$$

It is possible to do rotations around another axis or even multiple rotations around different axes by inserting a suitable rotation matrix in Eq.10 (assuming that the microscope employed is able to perform such scans).

The physical shift vector from Eq.10 for rotation α around the z axis is:

$$\begin{aligned} \mathbf{q}(\boldsymbol{\varrho}, \alpha) &= [\Delta x, \Delta y, \Delta z] \\ &= \boldsymbol{\varrho}\mathbf{S}\left(\mathbf{M}(\alpha)\right)^T \\ &= \begin{pmatrix} \Delta\xi \cdot s_\xi \\ \Delta\psi \cdot s_\psi \\ \Delta\zeta \cdot s_\zeta \end{pmatrix}^T \begin{pmatrix} \cos\alpha & \sin\alpha & 0 \\ -\sin\alpha & \cos\alpha & 0 \\ 0 & 0 & 1 \end{pmatrix} \\ &= \begin{pmatrix} \Delta\xi \cdot s_\xi \cdot \cos\alpha - \Delta\psi \cdot s_\psi \cdot \sin\alpha \\ \Delta\xi \cdot s_\xi \cdot \sin\alpha + \Delta\psi \cdot s_\psi \cdot \cos\alpha \\ \Delta\zeta \cdot s_\zeta \end{pmatrix}^T. \end{aligned}$$

It is easy to verify that when $\alpha = 0$, $\mathbf{M}$ reduces to the identity matrix and Eq.9 simplifies to Eq.6.

1.5 Scanning resolution

Changes in scanning resolution (7) or pixel dwell time τ_d (8) will alter the time delay function Eq.8 and result in different correlation curves. An example for scanning with double resolution but unchanged pixel dwell time τ_d in ξ axis is shown on Fig. S2B. An increased resolution increases the time taken to record a line and decreases pixel size. Therefore, in order to compare the CF for different resolutions it is more suitable to present them as functions of physical distance as is done in Fig. S2B.

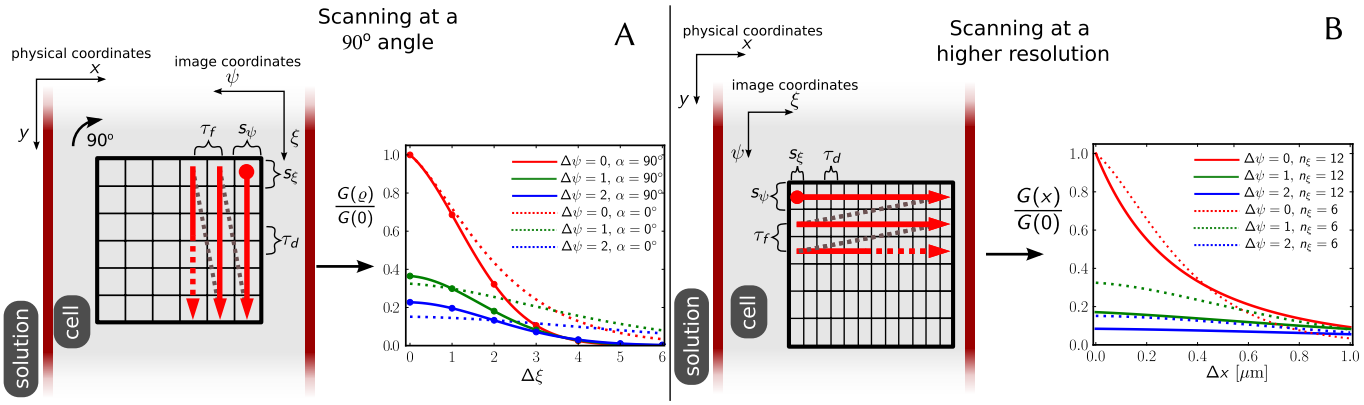

FIGURE S2: Modified scanning for RICS. (A) Scanning at an angle α rotates the image coordinates with respect to the physical coordinates and results in a different CF which can be used for determining anisotropy of diffusion. The CF for 0° angle scanning from Fig. S1B is shown in dotted lines and differs from the CF obtained for an image scanned at a different angle. In the shown example, scanning is performed at a 90° angle, effectively aligning the image ξ axis with the physical y axis and image ψ axis with physical x axis. (B) Changing the scanning resolution also alters the shape of the CF. In the example shown, the image is scanned at two times higher resolution resulting in the CF depicted with solid lines. Since the pixel dwell time τ_d is not changed, scanning one line takes two times longer. For comparison, the CF from Fig. S1B is shown in dotted lines. The horizontal axis now shows physical shift values in μm since the pixel size and count for the two CF-s is different.

1.6 Two diffusing species

It is possible for the fluorescent molecule to bind with other, larger, molecules in the intracellular solution. As a result, two subspecies of the fluorescent molecule would be diffusing in the cell: the faster unbound form and the slower bound form. Assuming that fluorescent properties of the dye are not altered as a result of binding and that the two species are non-interacting (i.e., the binding/unbinding is relatively slow), the CF for two species diffusing is (5, 9) :

$$G(\boldsymbol{\varrho},\alpha) = \frac{1}{\langle c_1(\mathbf{p}) + c_2(\mathbf{p})\rangle^2_{\mathbf{p}}} \cdot \iint W(\mathbf{r})W(\mathbf{r}')\left(\langle c_1\rangle \cdot g_{D1} + \langle c_2\rangle \cdot g_{D2}\right)\, \mathrm{d}\mathbf{r}\, \mathrm{d}\mathbf{r}', \tag{11}$$

where $\langle c_1\rangle$, $\langle c_2\rangle$ are concentrations of the two components and g_{D1} and g_{D2} are given by $G_{Dk}(\mathbf{r},\mathbf{r}',\boldsymbol{\varrho},\alpha)/\langle c_k\rangle$, ($k$ =1, 2). Inserting the gaussian PSF given in Eq.5 to calculate the CF for two components from Eq.11:

$$G(\boldsymbol{\varrho},\alpha) = \frac{1}{\left(\langle c_1\rangle + \langle c_2\rangle\right)^2} \cdot \left[\langle c_1\rangle \prod_{i=1}^{n} \frac{\exp\left(-\frac{q(\boldsymbol{\varrho},\alpha)_i^2}{4D_{1,i}t(\boldsymbol{\varrho})+w_i^2}\right)}{\sqrt{\pi\left(4D_{1,i}t(\boldsymbol{\varrho})+w_i^2\right)}} + \langle c_2\rangle \prod_{i=1}^{n} \frac{\exp\left(-\frac{q(\boldsymbol{\varrho},\alpha)_i^2}{4D_{2,i}t(\boldsymbol{\varrho})+w_i^2}\right)}{\sqrt{\pi\left(4D_{2,i}t(\boldsymbol{\varrho})+w_i^2\right)}}\right],$$

where $D_{1,i}$, $D_{2,i}$ are diffusion coefficients in direction i for the first and second component, respectively.

1.7 Triplet states

It is possible for a fluorescent molecule to go into a so-called triplet state from where it relaxes back to ground state after a delay much longer than it takes for the normal excitation-emission cycle to complete. This phenomenon, if ignored, could cause diffusion coefficients to be overestimated. To account for this effect, we multiply the CF function (Eq.9 or Eq. 11) with a compensation factor (4, 8–10) :

$$1 + \frac{T}{1-T}\exp\left(-\frac{t}{\tau}\right), \tag{12}$$

where T is the fraction of molecules in triplet state and τ the triplet state relaxation time.

1.8 Full form of correlation function

In this work the experimentally measured PSF was used instead of the approximated one (Eq.5), necessitating numerical integration for each CF evaluation:

$$G(\boldsymbol{\varrho},\alpha) = \frac{1}{\langle F_1(\mathbf{p}) + F_2(\mathbf{p})\rangle^2_{\mathbf{p}}}\left(1 + \frac{T}{1-T}\exp\left(-\frac{t}{\tau}\right)\right) \cdot \iint W(\mathbf{r})W(\mathbf{r}')\left(\langle c_1\rangle \cdot g_{D1} + \langle c_2\rangle \cdot g_{D2}\right)\, \mathrm{d}\mathbf{r}\, \mathrm{d}\mathbf{r}' \tag{13}$$

This is the CF form used for fitting experimental data in this work.

2 DETAILED METHODS

2.1 Confocal setup

To perform imaging for raster image correlation spectroscopy (RICS), we designed and built a confocal microscope. This allowed us to automate image acquisition under varying laser scanning angles and frequencies.

The confocal microscope was built around Olympus IX71-FVSF-2, using the left side port with the mounted scanning

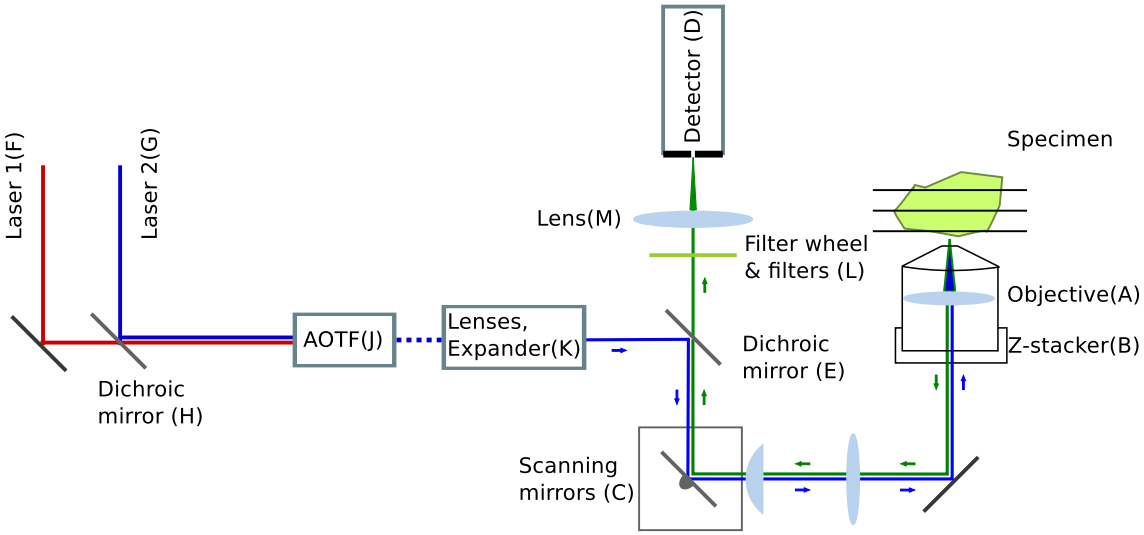

FIGURE S3: Scheme of the confocal microscope setup. See text for description of the parts.

lens (FV3-PLI2-2, Olympus). Images were acquired using water-immersion 60× objective (UPLSAPO, NA 1.2, Olympus, indicated by *A* on Fig. S3) mounted on piezoelectric objective-lens positioning system (MIPOS 250 SG driven by 12V40 CLE piezo amplifier, Piezosystem Jena, Germany, *B* on Fig. S3). Excitation laser beam was guided and fluorescence signal descanned (i.e., emitted light from the sample returns along the path taken by excitation light, reflecting from the scanning mirrors (*C*) before heading to the detector (*D*) from the dichroic mirror *E*) on the image plane of the scanning lens using galvo mirrors (6210H 3mm 6121H 2-mirror system, Cambridge Technology, MA, USA; *C* on Fig. S3).

Two lasers were used in the experiments: 633 nm 05-LHP-151 (Melles Griot, USA; *F* on Fig. S3) and 473 nm SDL-473-LN-O1OT (Shanghai Dream Lasers Technology Co. Ltd, China, *G* on Fig. S3). Beams of the lasers were combined using LM01-503 dichroic (Semrock, Rochester, NY, USA; *H* on Fig. S3); all following dichroics and filters are from this company), passed through an acousto-optical tunable filter (AOTF; *J* on Fig. S3) to select the laser line and regulate power of the excitation (AOTFnC-VIS-TN, AA Sa Opto-Electronic Division, France). Laser beam was expanded and filtered by spatial filter KT310 using C220TME-A (FD 11mm) as focusing lens, P25S (25 μm) pinhole, and LA1608-A (FD 75mm) as a collimating lens (all from Thorlabs, NJ, USA, *K* on Fig. S3). After the spatial filter, the beam was passed through iris SM1D12C (Thorlabs) set at 2.4 mm. Excitation light and fluorescence emission were separated by dichroic FF500/646-Di01-25x36 (*E* on Fig. S3). Fluorescence signal passed an emission filter (FF01-550/88-25 or FF01-725/150-25 for 473 nm or 633 nm excitation, respectively) which was selected using motorized filter wheel FW102B (Thorlabs; *L* on Fig. S3). After passing the emission filter, fluorescence signal was focussed by AC254-500-A1-ML (FD 500 mm; *M* on Fig. S3) on photon counter SPCM-AQRH-13 (PerkinElmer, USA; *D* on Fig. S3). In this design, photon counter detector (nominal diameter 170 μm) was used as a pinhole. The optical scheme was mounted on honeycomb table top 1HT12-15-20 positioned on pneumatic vibration isolation system 1VIS95-065-08-70 (Standa, Lithuania). The scheme was covered by custom cover with internal wall separating excitation light processing before the dichroic that splits excitation and emission light. To avoid signal contamination from emitted radiation by galvo mirrors, a wall was mounted that prevented the radiation to reach the detector from mirror motors. In addition, filter wheel LED position indicator was turned off during acquisition to avoid emission signal contamination. Optical scheme was adjusted to optimize for maximal emission signal and symmetry of point spread function (PSF). Resulting PSF has been published earlier (11).

Confocal microscope was controlled using custom made software. Galvo mirrors, piezoelectric objective-lens positioning system and AOTF were driven by PCIe-6259 (National Instruments, Texas, USA) using analog (mirrors and piezomotor) and digital outputs (AOTF). Feedback from galvo mirrors and piezomotor was recorded via analog input channels of the same card. This feedback signal was used to optimize the driving signal to ensure that the specified region of interest was scanned. Photon counter pulses were counted using PCI-6602 card (National Instruments) and read out by the software with the specified pixel time (1 μs for RICS measurements, 25 μs or larger for imaging). Excitation light was reduced during flyback using AOTF ensuring that it fully recovered by the beginning of each imaged line. The cards and the software was running on Linux (OpenSUSE) PC with National Instruments cards interfaced using NI-DAQmx 8.0.1 driver (National Instruments).

Imaging for RICS was performed in a $\sim$20×20 μm region with line scanning frequencies 167, 289, and 500 Hz. The signal was acquired during half of the scan time with the other half used for flyback. Imaging was performed with different scan directions by changing the angle of acquisition from -180° to +180° with a step of 20°. Images were acquired in sets of 90 (scanning frequency 500 Hz), 60 (289 Hz), and 30 (167 Hz) frames. The order with with images with different scanning frequencies and directions were recorded was randomized.

"Poking" of cells was performed with 1.0 mm diameter glass pipettes (World Precision Instruments, USA) manufactured

into 0.5 μm diameter tips using a pipette puller (PC-10 puller, Narishige, Japan). Cell membranes were permeated by controlling the pipette with a micromanipulator (PatchStar Micromanipulator System PS-8300C, Scientifica, England).

2.2 Determination of diffusion coefficients using RICS

Measurements were performed using different laser scanning frequencies and directions, similar to our earlier study (12). Through variation of scanning speed and direction, we change $t(\boldsymbol{\varrho})$. As a result, several components of diffusion coefficients can be estimated and fits can be optimized against measurements obtained with different scan frequencies. In total we used 19 angles spanning the range from 0 to 360 degrees and 3 different scanning speeds. In our analysis, we assumed that the shape of rat cardiomyocyte can be approximated as a cylindrical rod. In experiments, cells were aligned along the y axis. Thus, D_y corresponded to longitudinal diffusion coefficient D_L and $D_x = D_z$ — to the transverse one D_{TR}.

DCs, concentrations, and triplet state parameters were determined by fitting Eq. 13 with the correlation function estimated from measurements. Here, correlation between pixels on the same line as well as pixels on two adjacent lines was used. Fit was performed using the least squares method by the Levenberg-Marquardt algorithm (13). Integral in Eq. 13 was determined numerically to take into account the asymmetry of the PSF, as in (12). PSF measurements were conducted regularly so as to verify that it remains stable throughout the experiment series. Fits were performed with the PSF obtained for the current alignment.

Effect of fluorophore photobleaching can be compensated for by using the approach applied in (8, 14). This involves correcting the correlation curves obtained for the *i*-th image by multiplying it with the ratio of average intensity of the *i*-th image to that of the first image. We did not apply this correction, however, as we perform RICS analysis only to an subsection of the recorded images where the average image intensity did not change over time. This selectivity effectively means that a separate compensation factor is not necessary. Due to the high photostability of the dyes employed (as indicated by long stable ranges in image sequences) we considered triplet states as the main cause for loss of fluorescence that would interfere with DC estimation.

For calibration, the PSF was scaled with the scaling factor that was optimized together with other parameters when fitting the measurements recorded in water and solution. The scaling factor was found to be 1.042±0.014 (n=24). Value of 1.04 was used when analysing data recorded in cardiomyocytes.

When estimating DCs with RICS in cells, images are first processed by removing the immobile fraction of the signal using moving average, as in (2, 15). For that images were blurred with a 3x3 kernel (each pixel's value was taken as the average of the pixel together with its closest neighbors) to reduce interference with DC estimation (see *Supporting results*). This is similar to the approach used in (8).

2.3 Solutions

The measurement solution contained (in mM) 0.5 EGTA (Sigma, 03778), 3.0 KH_2PO_4 (Sigma, P0662), 3.0 $MgCl_2$ (Sigma, 63068), 20 HEPES (Sigma, H3375), 110 sucrose (Sigma, S1888), 20 taurine (Sigma, 86329), 0.5 dithiothreitol (Sigma, D0632) and 60 lactobionate (Sigma, L2398), 5 glutamate (Sigma, 49449), 2 malate (Sigma, M6413). In addition, 5 mg/ml BSA (Roche, 10 775 835 001) was added, and pH was adjusted at 25°C to 7.1 with KOH.

The simplified solution with reduced content of macromolecules contained (in mM) 0.5 EGTA, 3.0 KH_2PO_4, 3.0 $MgCl_2$, 20 HEPES, 0.5 dithiothreitol and 60 lactobionate. pH was adjusted at 25°C to 7.1 with KOH.

3 MATHEMATICAL MODEL

3.1 Relation of barrier permeability to barrier and molecule properties

Motivation. In our stochastic diffusion model we employ a permeability parameter p that describes the probability of a particle to traverse a barrier after coming into contact with it. This would, in reality, correspond to a distribution of permeable pores with a given radius on the surface of the barrier. If pore and particle dimensions are of the same order of magnitude then different particles would have different probabilities of being able to pass through the same pore, i.e., a permeability value of 1% for ATTO633-ATP would correspond to a smaller permeability for Alexa647-dextran 10K. Our goal is to determine the relative permeability values between particles of different sizes and to find a relationship between permeability and particle and pore dimensions.

Derivation. We take a circular object of radius r located at (x_r, y_r). The object is diffusing with diffusion coefficient D_x. Centered at $(0,0)$ is wall with an opening of radius R (see Fig. S4.)

The particle makes a random step, consisting of two independent steps in x and y directions : $dx \sim \mathcal{N}(0,\sigma)$ and $dy \sim \mathcal{N}(0,\sigma)$, where $\sigma = \sqrt{2\,D_x\,\tau}$. Total distance travelled $L = \sqrt{dx^2 + dy^2}$, follows the Rayleigh distribution:

$$L \sim Rayleigh(L,\sigma) = \frac{L}{\sigma^2}\exp\left(-\frac{L^2}{2\sigma^2}\right)$$

Probability of the particle passing through the hole is:

$$p_a = \frac{\int_{\alpha_1}^{\alpha_2}\int_{\frac{y_r}{\sin\alpha}}^{\infty} Rayleigh(L,\sigma)\,\mathrm{d}L\,\mathrm{d}\alpha}{\underbrace{\int_0^{2\pi}\int_0^{\infty} Rayleigh(L,\sigma)\,\mathrm{d}L\,\mathrm{d}\alpha}_{=1}}$$
$$= \frac{\int_{\alpha_1}^{\alpha_2}\exp\left(-\frac{y_r^2}{2\sigma^2\sin^2\alpha}\right)\,\mathrm{d}\alpha}{2\pi}\,, \qquad (14)$$

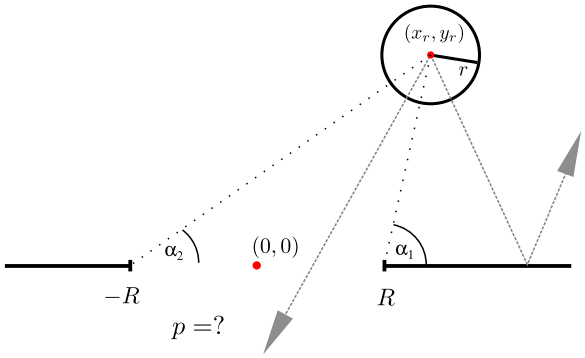

FIGURE S4: Probability p of particle of radius r located at x_r, y_r diffusing through a pore of radius R within timestep τ. α_1 and α_2 are the angles within which it is possible for the particle to permeate the pore (shown approximately on the figure)

where α_1 and α_2 are the minimum and maximum angles at which the object can still pass through the hole and $\frac{y_r}{\sin\alpha}$ is the minimal distance to travel to pass through at angle α. From Fig. S4 it is visible that α_1 and α_2 change as x_r, y_r, r and R change. It is possible to calculate α values iteratively with increasing accuracy or by numerically solving the exact equation relating all the parameters. The integral in Eq.14 can not be represented in elementary functions and we must calculate the probabilities we seek numerically. Example probabilities for ATTO633-ATP and Alexa647-dextran 10K are shown on Fig. S5. As can be seen, the probabilities for ATTO633-ATP compared to Alexa647-dextran 10K to go through the pore are greater at all locations.

The probability for a particle to get out from the inside of a square D with side length d covered with n pores of radius R on each side is:

$$P_a = \frac{4n \cdot \overbrace{\iint\limits_D p_a \,\mathrm{d}x_r \,\mathrm{d}y_r}^{\doteq Q}}{\iint\limits_D \mathrm{d}x_r \,\mathrm{d}y_r} = \frac{4n \cdot Q}{d^2}, \tag{15}$$

where Q is the value of the numerically calculated surface integral of p_a.

Probability P_a from Eq.15 gives the combined probability of a particle reaching the wall from anywhere inside the square and then passing through a pore, i.e., $P_a = p \cdot P_b$, where P_b is the probability of the particle reaching the wall, and p is the probability of permeating the wall (the barrier permeability parameter used in our stochastic diffusion model). In order to calculate P_b we first need to find the probability of reaching the wall from a given position (x_r, y_r). This is given by:

$$p_b = \frac{\int\limits_0^\pi \exp\left(-\frac{y_r^2}{2\sigma^2 \sin^2\alpha}\right) \,\mathrm{d}\alpha}{\int\limits_0^\pi \int\limits_0^\infty Rayleigh(L,\sigma) \,\mathrm{d}L \,\mathrm{d}\alpha} = \mathrm{erfc}\frac{y_r}{\sigma\sqrt{2}},$$

where erfc is the complementary error function. For P_b we get:

$$P_b = \frac{4 \cdot \iint p_b \,\mathrm{d}x_r \,\mathrm{d}y_r}{\iint \mathrm{d}x_r \,\mathrm{d}y_r} = \frac{4d\sigma\sqrt{\frac{2}{\pi}}}{d^2}. \tag{16}$$

Combining Eqs. 15 and 16 we get for permeability p:

$$p = \frac{P_a}{P_b} = \frac{nQ}{d\sigma\sqrt{\frac{2}{\pi}}}.$$

When we compare two molecules with different radii and diffusion coefficients (i.e., $r_1 \neq r_2$ and $\sigma_1 \neq \sigma_2$, whereby $Q_1 \neq Q_2$), then the ratio of their respective permeabilities is:

$$\frac{p_1}{p_2} = \frac{Q_1 \cdot \sigma_2}{Q_2 \cdot \sigma_1}. \tag{17}$$

The dependence of this ratio on pore radius R for ATTO633-ATP and Alexa647-dextran 10K is shown on Fig. S6. The fit depicted on the figure is: $\frac{p_1}{p_2} \approx \frac{R-r_1}{R-r_2}$. The fit can match the theoretical values closely and is trivial to calculate compared to finding exact theoretical values which require time consuming numerical calculations. The formula itself can be justified by the following: n pores of radius R on a otherwise impermeable line of length d gives $\frac{n \cdot R}{d}$ as the ratio of permeable to impermeable sections of the line i.e., permeability. For a particle with radius r the effective radius of a pore would be $R - r$, giving $\frac{n \cdot (R-r)}{d}$ as permeability. Introducing pore density $\eta = n/d$ we can write: $p = \eta(R - r)$. It is easy to see that using this result for two different particles and taking the ratio would yield the formula used for the fit in Fig. S6.

In two dimensions, total permeability for n circular pores of radius R on a surface with area A would be $\frac{n \cdot \pi R^2}{A}$. Again, for a particle this translates to effective permeability of $p = \frac{n \cdot \pi (R-r)^2}{A}$. Defining η as the number of pores per unit area, we get:

$$p = \eta \cdot \pi (R - r)^2,$$

which is the relationship between permeability, pore radius and particle radius used in our calculations.

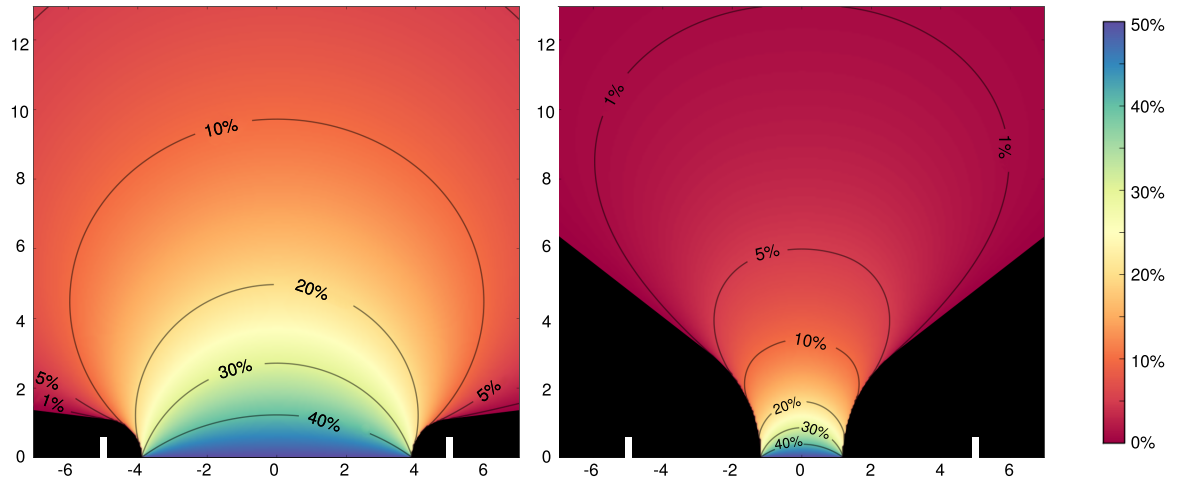

FIGURE S5: Probabilities for ATTO633-ATP (left) and Alexa647-dextran 10K (right) of going through a 10nm diameter pore (shown with white lines). Color at a given location indicates probability of the particle going through the pore in one random step. The area in black shows the region from where it is impossible for the particle to go through the pore.

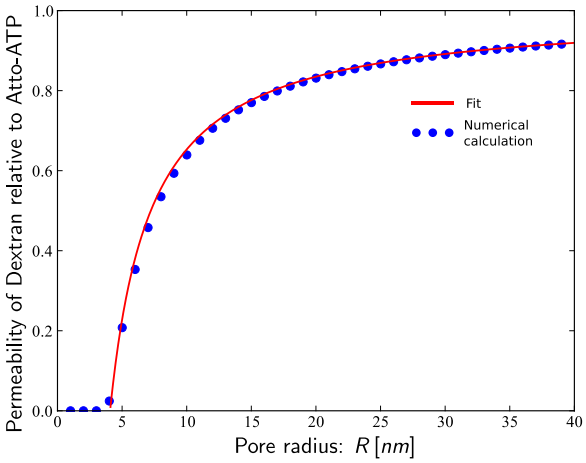

FIGURE S6: Ratio of probability of Alexa647-dextran 10K to ATTO633-ATP going through a pore of radius R. As pore radius increases, the ratio approaches 1, i.e., both particles are almost as like to permeate the pore. Dots indicate numerical calculations based on Eq.17, solid line is an approximate fit.

3.2 Theoretical correlation function for 1D RICS

In order to analyze images obtained from the simplified 1D stochastic diffusion model, an analytic expression for the correlation function is used in fitting. This is obtained for the 1D case from Eq.3. The correlation function showing correlation between pixels separated from each other by image shift $\Delta\xi$ and time t, can be calculated from:

$$G(\Delta\xi) = \frac{\int_{-\infty}^{\infty}\int_{-\infty}^{\infty} W(x_1)W(x_2)G_D(x_1,x_2,\Delta\xi)\,\mathrm{d}x_1\,\mathrm{d}x_2}{\left(\langle c\rangle \int_{-\infty}^{\infty} W(x)\,\mathrm{d}x\right)^2}\,.$$

Here, G_D is the correlation due to diffusion (from Eq.4 with $n = 1$)

$$G_D(x_1,x_2,\Delta\xi) = \frac{c}{\sqrt{4\pi\, D_x\, t}}\exp\left(-\frac{(x_2+\Delta\xi\cdot s_\xi - x_1)^2}{4iD_x\cdot t}\right)\,,$$

with $\langle c\rangle$ representing concentration. D_x the diffusion coefficient, s_ξ the pixel size in ξ direction and $t = t(\mathbf{\Delta}\xi)$ is the delay time between acquisition of two pixels separated by $\Delta\xi$.

W is the 1D PSF (from Eq.5 with $n = 1$):

$$W(x) = \exp\left(-\frac{2x^2}{w_x^2}\right),$$

where w_x determines the width of the PSF.

After taking all the integrals and similar to Eq.6 with $n = 1$:

$$G(\Delta\xi) = \frac{\exp\left(-\frac{(s_\xi\cdot\Delta\xi)^2}{4D_x\, t+w_x^2}\right)}{\langle c\rangle\sqrt{\pi}\sqrt{4D_x\, t + w_x^2}}\,.$$

This formula was used to fit numerical experiments performed with the 1D stochastic model.

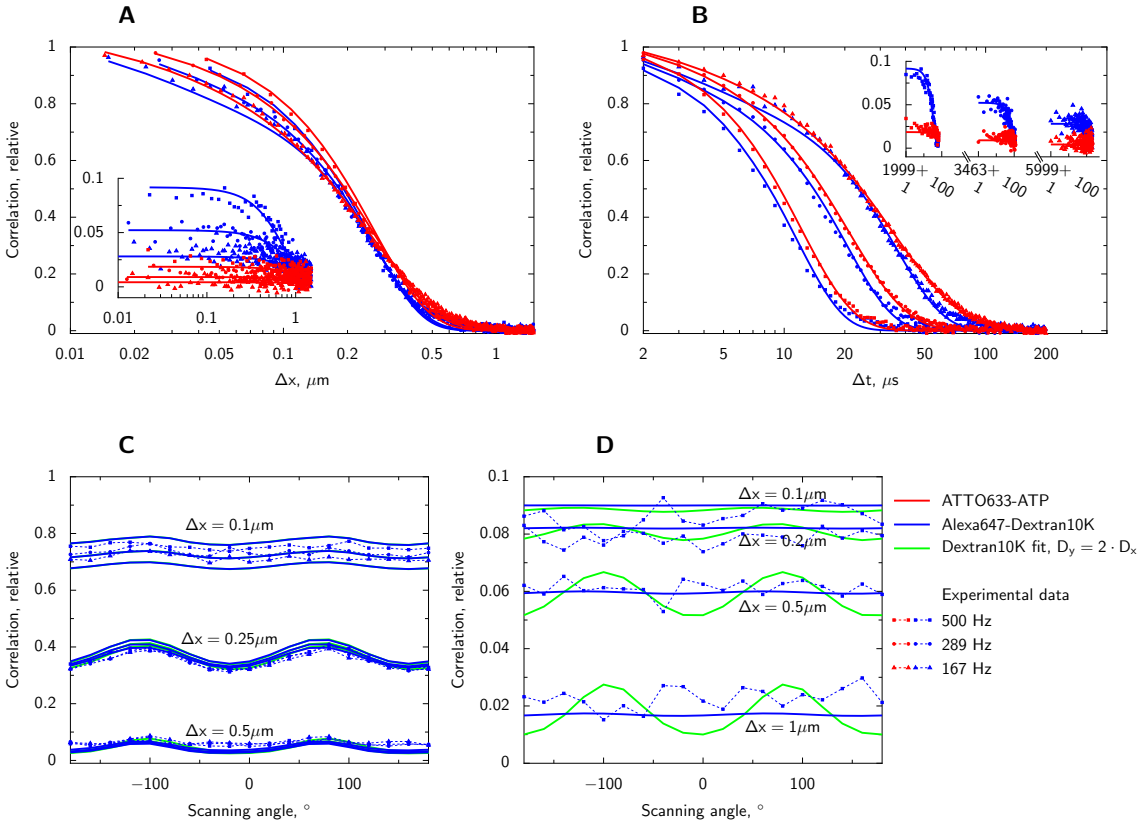

FIGURE S7: Diffusion of ATTO633-ATP (red) and Alexa647-dextran 10K (blue) in water analyzed by RICS. Experimental data (points) acquired at different laser scanning frequencies and directions are fitted with theoretical correlation curves given in Eq.13 (lines). By using dyes with different diffusion coefficients, we demonstrate the influence of diffusion coefficient on spatial (A) and temporal (B) components of correlation functions. Data and theoretical fits shown on A and B are identical. A is the classical way of presenting correlation functions in RICS analysis. As we use multiple scanning speeds, plotting correlation as a function of time (as in B) illustrates the differences caused by changes in scanning speed. Converting between A and B plots can be done by employing Eq.8. On A and B, imaging was performed with the laser scanning along a line parallel to axis x at different frequencies (frequencies noted in legend on the right bottom). Correlation along the same line is shown in the main graphs (A,B) while correlation of the signal between pixels in adjacent lines is shown in the insets. Due to the laser backtracking and variation in scan frequencies, temporal component has gaps visible in the inset of B. Due to asymmetry of PSF, laser scanning in different directions leads to modification of correlation function between pixels in the same line (C) and in the adjacent lines (D). This is demonstrated by showing correlation function estimated from the experiment (dots connected by dashed lines) and results of the fit (solid blue line) for Alexa647-dextran 10K. Correlation between pixels in the same line is not as sensitive to anisotropy of diffusion as correlation between neighbouring lines, resulting in an overlap between fits having a two time difference in diffusion coefficients in the y direction, as seen on C. Distinction between isotropic and anisotropic fits is mainly visible on correlation between pixels in adjacent lines (D).

4 SUPPORTING RESULTS

4.1 RICS extensions

To demonstrate the extended RICS protocol, we determined diffusion coefficients (DCs) of fluorescent dyes in water. Representative correlation functions (CF) calculated from measurements of ATTO633-ATP and Alexa647-dextran 10K are shown in Fig. S7. By varying the frequency of laser scanning while acquiring images in confocal microscope, we varied the relationship between spatial and temporal components of fluctuations of the signal (Fig. S7A and B). The plots in Fig. S7A and B contain the same data and theoretical fits. However, since we alter the scanning frequency it is easier to visually discern the differences in correlation if it is shown as a function of time (Fig. S7B) rather than space (Fig. S7A), which is the classical representation for RICS. In both cases Eq.13 was used for the theoretical fit. While for Alexa647-dextran 10K a significant correlation of fluorescence fluctuations can be observed between pixels in two consecutive scan lines (Fig. S7A and B insets), the correlation is rather small for ATTO633-ATP. This is due to the larger DC of ATTO633-ATP leading to a smaller probability of a molecule staying in the same neighborhood while the laser is scanning two consecutive lines. For Alexa647-dextran 10K, correlation of fluctuations between pixels depends on laser scanning frequency, as demonstrated in Fig. S7A and B insets. By taking into account asymmetry of the point spread function (PSF), we can fit CFs obtained from measurements at different laser scanning frequencies and directions with a theoretical CF from Eq.13 . The resulting fits are represented in Fig. S7 by solid lines. From analysis of the CFs for Alexa647-dextran 10K in water, dependence of CF on scanning angle in Fig. S7C and D demonstrates that asymmetry of PSF is mainly influencing correlation between pixels in the same line of an image. When fitting the CFs with a model that assumes a two time difference in DCs in x and y direc-

tions (green solid line in Fig. S7C and D), we observed that the model solution was different from isotropic case mainly in the signal correlation between pixels in adjacent lines (Fig. S7D). Correlation of the signal in the same line was not that much influenced by anisotropy (green and blue lines in Fig. S7C are very close to each other). Note that this observation can depend on the DCs.

Obtained diffusion coefficients, triplet time constants (τ) and triplet state contribution (T) to correlation functions for ATTO655-COOH, ATTO633-ATP, and Alexa647-dextran 10K are shown in Table 1 (main text). To test our method, we analyzed diffusion of ATTO655-COOH in water at 26°C. According to our measurements, the DC for ATTO655-COOH is 454±3 μm^2/s. This is similar to the DC in water determined for the same dye using 2-focal fluorescence correlation spectroscopy measurements (16), 426±8 μm^2/s at 25°C. Taking into account the difference in temperatures, this would correspond to ∼437 μm^2/s in our conditions. DCs for ATTO633-ATP and Alexa647-dextran 10K which we used to study diffusion in cardiomyocytes (CM) were smaller in water as well as in the measurement solution (Table 1). Comparing DCs in water and solution, we can see that exposure to solution reduces the DC of Alexa647-dextran 10K and ATTO655-COOH to 80-85% of the value in pure water. For ATTO633-ATP, the reduction is considerably larger: DC in solution was only 60% of the value in water. We checked whether this reduction of DC could be attributed to the binding of a fraction of ATTO633-ATP to proteins in measurement solution. However, RICS analysis was not able to resolve two components (slow and fast) of ATTO633-ATP (both components had the same DC when the slow component's DC was not limited). However, when exposed to a simplified solution with a reduced amount of macromolecules (see *Detailed Methods* of Supporting Material for solution composition), we observed a reduction of the DC of ATTO633-ATP to 265±10 μm^2/s ($n = 4$), i.e., to ∼80% of the value in water. In contrast, the DCs of Alexa647-dextran 10K and ATTO655-COOH in this simplified solution remained similar to their DCs in water : 60±1 ($n = 4$) μm^2/s and 451±10 μm^2/s ($n = 5$), respectively. This suggests that diffusion of ATTO633-ATP in the measurement solution is influenced in part by interaction of ATTO633-ATP salt with ions in the solution, leading to an increase in the apparent hydrodynamic radius of ATTO633-ATP. To avoid any bias induced by such interaction, we compared the DCs of dyes in the cell to the DCs in the measurement solution, not to the coefficients in water.

We fitted the CFs estimated from the measurements in water and solution using the anisotropic model. According to our fits, DCs in longitudinal y (L) direction was systematically overestimated (Table 1) leading to up to 22% difference in DCs (the largest anisotropy was estimated for ATTO633-ATP in solution). Thus, small differences in DCs due to anisotropy cannot be resolved with our method. We found that the predicted anisotropy can depend on the model used. In estimating DCs, we used a model where the x and z direction were taken to represent the transverse TR direction. When taking y and z as the transverse direction instead, the predicted anisotropy was much smaller. The exception was a relatively high anisotropy predicted for Alexa647-dextran 10K in water (25%). We think that such dependence on the model is induced by inaccuracies in the PSF.

When estimating DCs with RICS in cells, images are first processed by removing the immobile fraction of the signal using a moving average. We applied the same pre-processing to images recorded in water and solution. As a result, we found that such pre-processing affects RICS analysis. Influence on DC was found to be relatively small with DC estimated after removal of the average being 0.95× to 1.13× larger than DC estimated from the original images. However, triplet state characteristics were influenced more profoundly with triplet state time constant increasing by 1.17× to 1.52× and triplet state contribution increasing by 1.05× to 1.36×. To reduce the influence of pre-processing on RICS analysis, we took advantage of sub-PSF pixel sizes and performed averaging by using images blurred with a 3x3 kernel (each pixel's value was taken as the average of the pixel together with its closest neighbors). Using such a kernel reduced the influence of average signal subtraction on DC (1.02× to 1.05× larger than before pre-processing), triplet state time constant (1.08× to 1.16×),

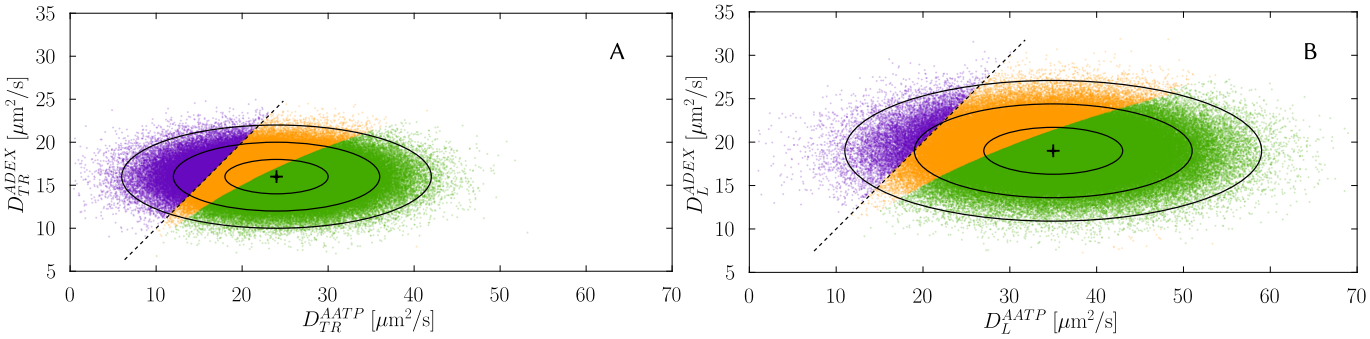

FIGURE S8: Distributions of random generated pairs of ATTO633-ATP and Alexa647-dextran 10K diffusion coefficients in transverse(A) and longitudinal directions (300000 values each). Pairs were randomly generated from normal distributions having the mean and standard deviation obtained from experiment (shown in Table 1 of the main text. Experimental mean values are shown with a cross. Ellipses indicate distances 1,2 and 3 standard deviations from the mean. Dotted line show DC values of ATTO633-ATP and Alexa647-dextran 10K are equal. As explained in the text, values left of this line are discarded and not included in analysis. The middle region(shown in yellow) contains DC value pairs where density of pores in barrier would be less then 1 per barrier. For the DC values in the green region intersections are found as in the main text and collected for statistics.

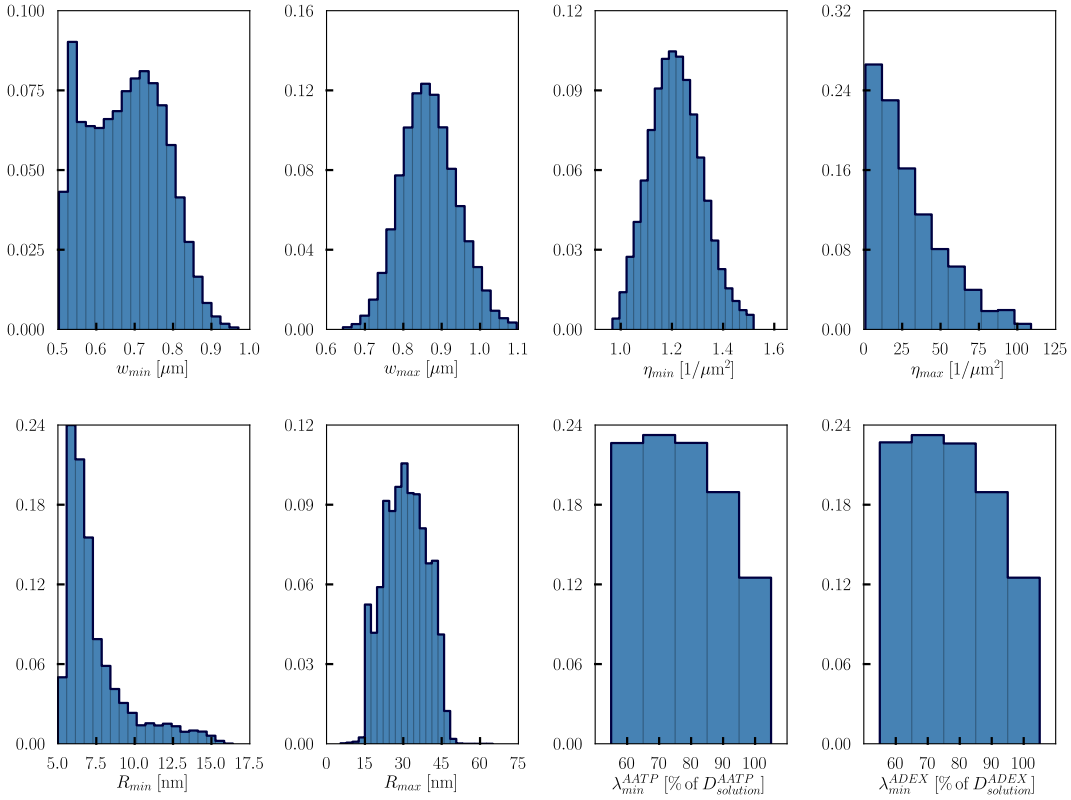

FIGURE S9: Histograms showing distributions of minimum and maximum model parameter values obtained from Monte Carlo simulations in the transverse direction.

and triplet state contribution (0.92× to 1.04×). On the basis of these observations, we used blurring by 3x3 kernel in analysis of diffusion in cardiomyocytes.

4.2 Diffusion obstacle parameter sensitivity

Parameters presented in Table 2 of the main text were obtained by finding intersections between curves of experimental and computational results. As visible from Figures 2C,2D and 2E in the main text, a range of barrier-to-barrier distance, pore radius and pore density values satisfy the constraints of the model and computational results. The experimentally obtained DC values have a error associated with them. In order to estimate the uncertainties caused by measurement errors in the parameters we found, Monte Carlo analysis was applied. Similar to the procedure depicted on Figure 2B and 2C, random DC for ATTO633-ATP and Alexa647-dextran 10K were chosen from a normal distribution with the mean and standard deviation equal to the values from experiments presented in Table 1 (i.e., $\mathcal{N}(24,6)$, $\mathcal{N}(16,2)$ for ATTO633-ATP and Alexa647-dextran 10K in the transverse direction and $\mathcal{N}(35,8)$, $\mathcal{N}(19,3)$ in the longitudinal direction). For each randomly generated ATTO633-ATP Alexa647-dextran 10K DC value pair, intersections were found and from those a range of suitable parameter values determined. Random sampling was performed 300000 times for both transverse and longitudinal directions. The resulting distribution of random DC value pairs are shown on Fig. S8A and B for the transverse and longitudinal directions, respectively. Of possible combinations two types were discarded. First, cases where DC of Alexa647-dextran 10K was larger than ATTO633-ATP (left of the dashed lines and on Fig. S8) and, secondly, cases where the pore density value was so low that less than one would be present on a single barrier element (the middle, light region on Fig. S8). For all other pairs model parameter maximum and minimum values were obtained and collected. Histograms for obtained maximum and minimum parameter values are presented in Figs. S9 and S10. Histograms for maximum estimate of DC reduction values are not shown as they were always 100% of the DC in solution. The results presented in Table 2 in the main text are the mean and standard deviations of these distributions.

SUPPORTING REFERENCES

1. Brown, C. M., R. B. Dalal, B. Hebert, M. A. Digman, A. R. Horwitz, and E. Gratton, 2008. Raster image correlation spectroscopy (RICS) for measuring fast protein dynamics and concentrations with a commercial laser scanning confocal microscope. *J Microsc* 229:78–91.
2. Digman, M. A., C. M. Brown, P. Sengupta, P. W. Wiseman, A. R. Horwitz, and E. Gratton, 2005. Measuring fast dynamics in solutions and cells with a laser scanning microscope. *Biophys J* 89:1317–1327.
3. Digman, M. A., and E. Gratton, 2011. Lessons in Fluctuation Correlation Spectroscopy. *Annu Rev Phys Chem* 62:645–668.
4. Haustein, E., and P. Schwille, 2007. Fluorescence correlation spectroscopy: novel variations of an established technique. *Annu. Rev. Biophys. Biomol. Struct.* 36:151–169.
5. Lakowicz, J., 2006. Principles of fluorescence spectroscopy. Springer.
6. Thompson, N., 2002. Fluorescence Correlation Spectroscopy. *In* J. Lakowicz, C. D. Geddes, and J. R. Lakowicz, editors, Topics

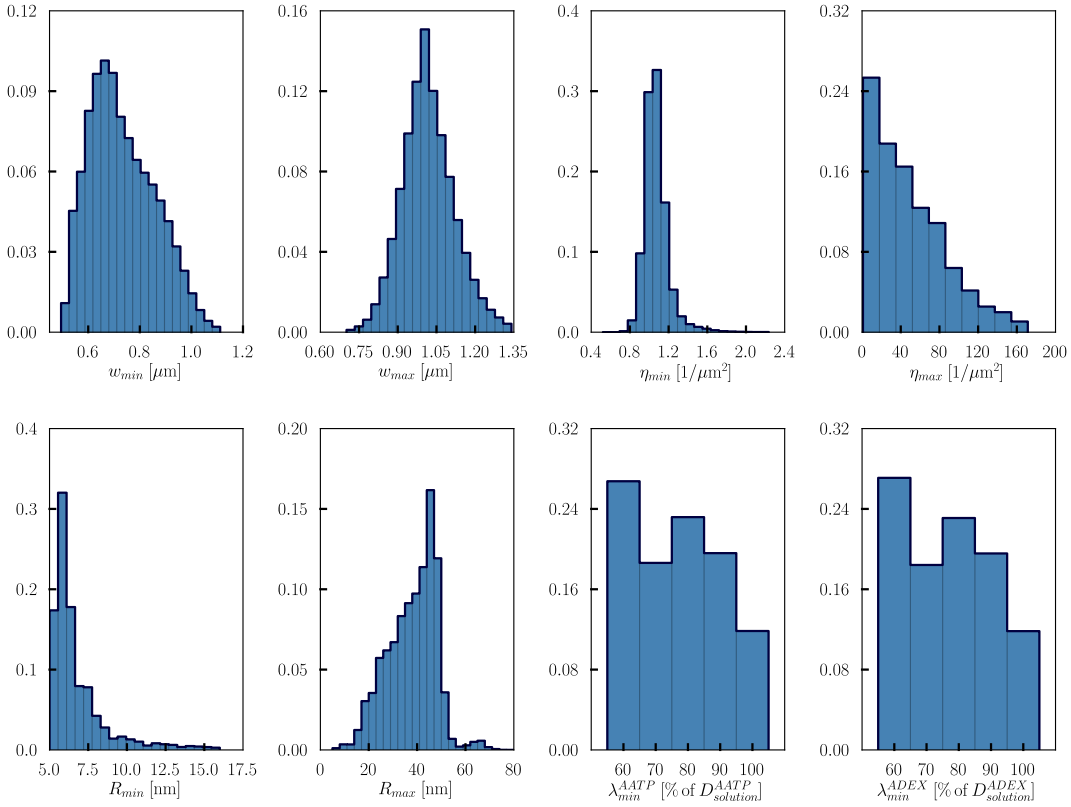

FIGURE S10: Histograms showing distributions of minimum and maximum model parameter values obtained from Monte Carlo simulations in the longitudinal direction.

in Fluorescence Spectroscopy, Springer US, volume 1 of *Topics in Fluorescence Spectroscopy*, 337–378.

7. Vendelin, M., and R. Birkedal, 2008. Anisotropic diffusion of fluorescently labeled ATP in rat cardiomyocytes determined by raster image correlation spectroscopy. *Am. J. Physiol. Cell. Physiol.* 295:C1302–1315.
8. Gröner, N., J. Capoulade, C. Cremer, and M. Wachsmuth, 2010. Measuring and imaging diffusion with multiple scan speed image correlation spectroscopy. *Opt. Express* 18:21225.
9. Krichevsky, O., and G. Bonnet, 2002. Fluorescence correlation spectroscopy: the technique and its applications. *Reports on Progress in Physics* 65:251.
10. Widengren, J., U. Mets, and R. Rigler, 1995. Fluorescence correlation spectroscopy of triplet states in solution: a theoretical and experimental study. *J Phys Chem* 99:13368–13379.
11. Laasmaa, M., M. Vendelin, and P. Peterson, 2011. Application of regularized Richardson-Lucy algorithm for deconvolution of confocal microscopy images. *J Microsc* 243:124–140.
12. Vendelin, M., and R. Birkedal, 2008. Anisotropic diffusion of fluorescently labeled ATP in rat cardiomyocytes determined by raster image correlation spectroscopy. *Am J Physiol Cell Physiol* 295:C1302–C1315.
13. Moré, J. J., D. C. Sorensen, K. E. Hillstrom, and B. S. Garbow, 1984. The MINPACK Project. *In* W. J. Cowell, editor, Sources and Development of Mathematical Software, Prentice-Hall.
14. Brown, C. M., R. B. Dalal, B. Hebert, M. A. Digman, A. R. Horwitz, and E. Gratton, 2008. Raster image correlation spectroscopy (RICS) for measuring fast protein dynamics and concentrations with a commercial laser scanning confocal microscope. *J. Microsc.* 229:78–91.
15. Rossow, M. J., J. M. Sasaki, M. A. Digman, and E. Gratton, 2010. Raster image correlation spectroscopy in live cells. *Nat Protoc* 5:1761–1774.
16. Dertinger, T., V. Pacheco, I. von der Hocht, R. Hartmann, I. Gregor, and J. Enderlein, 2007. Two-focus fluorescence correlation spectroscopy: a new tool for accurate and absolute diffusion measurements. *Chemphyschem* 8:433–443.